# Hot Electron Temperature Layer in the Martian Atmosphere

Andersson L.[1], C. M. Fowler[2], R. E. Ergun[1], S. W. Stone[3], R. Yelle[3], T. E. Cravens[4], E. Thiemann[1], M. Pilinski[1], W. K Peterson[1], A. Nagy[5], S. Bougher[5], M. Benna[6], D. Mitchell[2] and J. McFadden[2]

[1]Laboratory for Atmospheric and Space Physics, Univ. of Colorado, Boulder, CO, USA
[2]Space Sciences Laboratory, U.C. Berkeley, Berkeley, CA, USA
[3]Lunar and Planetary Laboratory, University of Arizona, Tucson, AZ, USA.
[4]U. Kansas, Lawrence, KS, USA
[5]CLaSP Department, University of Michigan, Ann Arbor, MI, USA.
[6]NASA/GSFC, Greenbelt, MD, USA

Corresponding author: first and last name (laila.andersson@lasp.colorado.edu)

**Abstract**

The MAVEN mission has measured an electron temperature spike at altitudes where the Martian atmosphere becomes optically thick and changes occur in the atmospheric chemistry. The temperature spike is consistent from orbit to orbit, but changes in location based on solar zenith angle (SZA) and has only been observed for SZA <80$^o$. This letter presents the conditions under which it is observed and discusses possible sources. The electron temperature spike seems to be co-located with a temperature dip in the neutral atmosphere. The observed temperature spike/dip might be indicative of an inversion layer in the Martian atmosphere. The altitude location of the electron temperature spike is in the lower dynamo region where the electrons start to be unmagnetized. The observations are unlikely to be significant for overall Martian plasma dynamics, but are a clear indication that the large-scale Martian atmosphere is still not completely understood.

## 1 Introduction

In-situ measurements of planetary atmospheres and ionospheres other than Earth's are rare. Despite a plethora of probes having visited Mars over time, the Viking landers were the only two missions to obtain in-situ measurements of the electron temperature ($T_e$) [Hanson and Mantas, 1988] prior to the arrival of the Mars Atmosphere and Volatile EvolutioN (MAVEN) mission in 2014 [Jakosky et al., 2015]. The Viking landers each measured one $T_e$ profile during descent, down to altitudes of about 200 km. By contrast, MAVEN measures two profiles (inbound and outbound) per periapsis pass (once every ~4.5 hours) down to around 150 km altitude during normal operation. One long-standing question for Mars aeronomy is to understand what drives $T_e$ in the lower ionosphere. The Viking $T_e$ profiles (and now MAVEN profiles as well) demonstrate that additional heating is required to validate models of known heating and loss sources, with observations, particularly in the topside ionosphere [Chen et al., 1978; Rohrbaugh et al., 1979; Ergun et al., 2015; Sakai et al., 2016]. The altitude at which $T_e$ approaches the neutral temperature is also unclear and this region is below the measurement altitude range of MAVEN. Understanding $T_e$ is important because it drives ion loss through ambipolar electric fields [Schunk and Nagy, 1980; Ergun et al. 2015] and controls whether the atmospheric loss of oxygen occurs via ions or through neutrals [Ergun et al., 2016] as a result of dissociative recombination of $O_2^+$ [Schunk and Nagy, 1980].

Modeling $T_e$ is difficult and thus it is often prescribed in some models rather than solved self-consistently [e.g. Andersson et al., 2010; Andersson and Ergun, 2012; Ma et al., 2017]. Most models of $T_e$ at Mars tend to be 1-D [Chen et al., 1978; Rohrbaugh et al., 1979], and are still unable to fully explain the observed $T_e$ altitude profiles [Sakai et al., 2016]. Using the $T_e$ measurements from the MAVEN mission, attempts have been made to quantify the importance of the different heat sinks and sources [Peterson et al., 2016]. However, only limited magnetic field orientations and solar zenith angles (SZA) have been evaluated successfully. At the sub-solar region, the largest energy source is from solar EUV heating, resulting in large neutral atmospheric scale heights and ionospheric densities in this region. These quantities decrease with increasing SZA, with the nightside ionospheric density being 1-3 orders of magnitude less dense than at the sub-solar point. The Martian neutral atmosphere and ionosphere are highly variable and closely coupled, making it important to provide the ionospheric density with respect to the neutral densities.

Heating of electrons in the ionosphere is dominated by photoelectron production [Schunk and Nagy, 1980]. The hot energy tail of the photoelectrons interacts with the cold bulk electron

population resulting in a loss of energy in the tail and a heating of the bulk population. The major cooling of the bulk electron population is via collisions with various neutral species and ions, and at Mars the electron cooling rate, at lower altitudes, is dominated by the vibrational excitation of $CO_2$ [Schunk and Nagy, 1980; Strangeway, 1996]. Thermal conduction also plays an important role in controlling $T_e$ at higher altitudes.

In this letter, we report a $T_e$ spike observed by the MAVEN spacecraft below 160 km altitude. Although this spike was first observed earlier in the mission, it is only until recently that enough observations were acquired to perform detailed analysis on the spike. The observations presented indicate that we do not yet fully understand important ionospheric/atmospheric processes at Mars. In Section 2 we present the $T_e$ observations and put them into context with other atmospheric quantities. In Section 3 energy sources and sinks that impact $T_e$ at Mars are discussed and the most likely cause of the observed temperature spike suggested.

## 2 Observations

The MAVEN satellite orbiting Mars is designed to measure the upper atmosphere [Jakosky et al., 2015]. The spacecraft periapsis altitude is usually determined by a density corridor such that spacecraft drag at periapsis does not exceed specified limits. For roughly a week at a time on nine different occasions the periapsis has been lowered for nine "deep dip" (DD) campaigns. These DDs were performed at different locations at Mars and this study focuses on the four DDs that are closest to the subsolar point, as shown in Table 1. The orbit location presented in Table 1 is based on the altitudes sampled below 160 km. These are the altitudes where the neutral temperature has the largest gradient with respect to altitude and the location where maximum energy deposition from solar extreme ultraviolet (EUV) radiation takes place.

The DD closest to the subsolar point was performed in April of 2015 (DD2) and a temperature spike was observed on every periapsis segment throughout the DD week at roughly the same altitude. Figure 1 shows an altitude profile of $T_e$ for one of the outbound passes presented in panel a, as measured by the Langmuir Probe and Waves (LPW) instrument [Andersson et al., 2015]. Resolving low $T_e$ with any Langmuir probe is difficult and the LPW instrument is capable of resolving $T_e$ down to an instrumental lower limit of around 400-600$^o$K. The $T_e$ is derived from the measured current-voltage (IV) curve of the LPW instrument. The region of the IV-curve where $T_e$ are derived from is presented in panels b and c of Figure 1. Three IV-curves are shown in panel b, color coded by the altitude at which they were measured as presented by the horizontal lines in panel a. The electron density ($N_e$) changes over the displayed altitude region but as can be seen, $T_e$ at the temperature peak (green line) is clearly different from the IV-curves taken from above and below the peak (blue and red line overlapping lines). The size of the crosses in the figure demonstrate the approximate uncertainty in measured currents and applied voltages. The sweep is obtained over a finite period of time (one to four seconds for LPW at periapsis depending on operation mode), therefore rapid changes in plasma conditions that occur on timescales smaller than the sweep time can lead to large uncertainties in derived quantities (i.e. $N_e$ and $T_e$). Plasma conditions are typically constant at periapsis during DD conditions because the spacecraft flies with the most conducting spacecraft side exposed to the plasma flow (the RAM side). As a result, the spacecraft potential is steady across multiple instrument sweeps resulting in a negligible uncertainty.

Modeled IV-curves under identical plasma density but different $T_e$ are shown in panel c. The green curve is modeled for plasma conditions identical to those observed at the temperature peak ($N_e$ ~15,800 /cc, $T_e$ ~1100 K; the purple and orange curves in panel c are modeled for lower $T_e$ (600 and 800 K) and demonstrate that the LPW instrument can clearly resolve the observed temperature spike.

The averaged $T_e$ profile from DD2 was analyzed by Ergun et al. [2015], but in that paper the $T_e$ spike was ignored due to a lack of an explanation at that time. The neutral and plasma parameters during DD2 were fairly constant [Bougher et al., 2015], making it difficult to converge on a definitive cause of the observed temperature spikes. During 2017-2018, new DDs at low (but different) SZA have been performed, allowing us to analyze the $T_e$ spike in greater detail. These new DDs are described in Table 1 and a $T_e$ spike for all DD periods with SZA <80$^o$ is observed by MAVEN. DD7, which was executed at the dusk terminator is included as a reference period where no $T_e$ spike was observed.

To compare the different DDs, information from Solar Wind Electron Analyzer (SWEA) [Mitchell et al., 2016], the Extreme ultraviolet monitor (EUVM) [Epavier et al., 2015], Neutral Gas and Ion Mass Spectrometer (NGIMS) [Mahaffy et al., 2014], and Magnetic field instrument (MAG) [Connerney et al., 2015] results have been analyzed. The energy input can be estimated using the EUVM intensity and the SWEA electron flux from different energy ranges. The energy loss can be inferred from the NGIMS neutral and ion density observations. In magnetized plasma, heat transport is controlled by magnetic field information observed by the MAG instrument.

A statistical analysis of $T_e$ has been undertaken to determine the cause of the observed $T_e$ spike, and the results of this analysis are presented in Figure 2. Altitude profiles are presented in the top and the bottom row of Figure 2, while the middle row shows different densities as a function of the $T_e$ on the x-axis. The altitude of the data presented here is the aerodetic altitude in the International Astronomical Union (IAU) frame. The different DDs, DD2, DD8, DD9, and DD7 are respectively color coded with the following colors black, green, red and pink. DD8 and DD9 (red and green) show almost the same trends. Therefore, in the text below only DD8 will be mentioned. As mentioned earlier, DD7 (pink information) is included to show an example where no $T_e$ spike was observed.

The information in Figure 2 is either shown as dots or lines. The dots are all individual measurement from the full time period of each DD. Since $T_e$ increases with altitude the data presented in Figure 2 is limited to the lower altitudes omitting the high altitudes where $T_e$ starts to be comparable to or exceed the maximum $T_e$ in the $T_e$ spike. Therefore, the upper altitude cutoff in Figure 2 is different for each DD. The solid lines shown in Figure 2 represent the average value derived using an altitude resolution of 2 km. Each measurement has an uncertainty/error associated with it but this is not taken into consideration when deriving the altitude profiles. This will affect, for instance, the $T_e$, since this derived quantity has an asymmetric uncertainty; an uncertainty which is larger on the lower temperature side. Since the discussion below is more about the trends rather the exact values, this omission will not impact the result of the letter. The following text will discuss the panels of Figure 2 one at the time and their implication.

The key observation is the $T_e$ presented in Figure 2b. The full width of the $T_e$ spike is indicated by the black(green) dotted lines for DD2(DD8). These horizontal lines are reproduced in all panels in

Figure 2 which are presented as function of altitude. The $T_e$ spike for DD2 is located at a fairly fixed altitude throughout the DD-week resulting in a clear spike in Figure 2b. For DD8(DD9) the altitude location of the $T_e$ spike from each individual orbit varies slightly over the DD-week resulting in a wider, less sharp, spike as seen in the green and red lines.

The half-width and the size of each spike is presented in Table 1. One can question if the true $T_e$ spike for DD2 is larger than that presented in Table 1. The issue is that on either side (altitudes above and below) of the $T_e$ spike, the temperature is almost ~700 K. This baseline from which the $T_e$ spike is referenced could be the true temperature but it is also possible that the instrument is reaching its low temperature limit. As mentioned earlier, all LP's have a lower temperature where the instrument noise and the sensor surface inhomogeneity prevents lower temperatures from being observed. However, for the three DD occurring two years later the instrument can derive colder temperatures indicating DD2 is most likely presented correctly. If there is a change in the instrument lower limit it could only be explained by changes in surface properties of the sensor. For the purpose of this paper, the exact lower temperatures at which the instrument can no longer derive an accurate $T_e$ is not important. The $T_e$ spike is clear and not an effect of deriving $T_e$; though it is possible that the amplitude of the spike is underestimated.

The average electron density profiles are presented in Figure 2a by the solid lines. For the DD with SZA $<80^o$ the MAVEN satellite did not clearly pass below the peak in the electron density as can be seen by the continuous increase in density with decreasing altitude. For the terminator, DD7, the satellite measured well below the electron density peak and the densities below ~150 km are much smaller compare to the other DD's.

One heat source for the bulk electrons is the high energy tail of the electrons (suprathermal component). As the suprathermal electron components lose their energy, the flux levels at the lower energies increases. Due to the composition of the Mars ionosphere electrons around 1-3 eV are lost efficiently to the neutrals resulting in low electron cut-off in the flux at these energies. Using SWEA data, the integrated flux levels for 3-6 eV electrons, which are above the cut-off energy, are derived and presented as the dots in Figure 2a. The flux levels presented are scaled in Figure 2a allowing the electron flux to be presented together with the electron density. As can be seen, within each DD-week the shape as function of altitude is fairly consistent. At high altitude with fewer collisions, the 3-6 eV flux increases with decreasing altitude and increasing neutral density as expected. When the neutral collision frequency starts to dominate the energy transfer, the suprathermal component flux levels start to decrease rapidly with decreasing altitude. The altitude where this turnaround is located is approximately the altitude of the $T_e$ spike. However, there is no indication that this suprathermal electron component could be the cause of the narrow $T_e$ spike.

The main heat source for $T_e$ is the solar EUV and the subsequent photoelectrons, both presented in Figure 2c. The energy deposition by the EUV on the measured $CO_2$ atmosphere is presented by the solid lines. Using the EUVM data the full wavelength spectrum is derived and applied to the absorption cross-sections. The neutral density ($N_n$) profile is based on the local $CO_2$, $N_2$ and $O$ densities assuming a spherical symmetric atmosphere (using only inbound data). The spherical symmetric assumption is not a concern for small SZA but will impact the result at large SZA (i.e. DD7). How effective the energy deposition is in heating the electrons is not completely known. But the key observation here is that no variations in heating is observed at the location of the $T_e$

spike demonstrating that the EUV energy deposition alone cannot explain the spike. Note also that the $T_e$ spike location is where the atmosphere starts to be optically thick, indicating that the importance of photochemical reactions is changing in this altitude region. For DD7, which is at the terminator, the energy deposition line is just a guideline below ~155 km due to the large SZA.

The solar EUV intensity changed between 2015 and 2017. This can be seen in all three panels Figure 2a to 2c. Therefore, any differences between DD2 and the other DDs might just be an effect of different EUV intensities and not necessarily due to SZA effects. For this letter, we will assume both contribute to the changes but will not quantify how much of the difference is due to SZA effects versus different energy inputs.

The peak in photoelectrons produced at Mars are mainly 23 eV and the 27 eV [Frahm et al., 2006]. The integrated electron flux levels for the 20-30 eV SWEA spectrum are presented as dots in Figure 2c. As in Figure 2a, the electron flux levels in Figure 2c are scaled to allowed them to be presented together with the solar energy deposition. That the solar input is not changing significantly during each week can be seen at the higher altitudes (>155 km) where the integrated 20-30 eV flux levels are very well confined to a constant value. At lower altitudes, the absorption of EUV results in a quite rapid decreases in photoelectrons production.

There is no indication that either the photoelectrons or the energy deposited from EUV are the source of the locally confined $T_e$ spike. There are other sources of energy in the atmosphere such as precipitating protons from the plasma and charge exchange with particles moving from the solar wind into the atmosphere as neutrals (where they can then charge exchange a second time and can be observed as protons) [Halekas et al., 2015]. These particles start to deposit their energy at approximately the altitude of the observed $T_e$ spike. DD2 had such a precipitating population present, but not DD7, demonstrating that they alone cannot explain the $T_e$ spike. Also, the amount of energy available to the electrons is small in these cases. Therefore, none of the heat sources analyzed can explain the observed $T_e$ spikes.

In the atmosphere, many processes are organized by pressure. Different densities of $N_e$, $O_2^+$ and $CO_2$ as function of $T_e$ are presented in Figure 2d to 2f as proxies for various pressure coordinates. To mimic the altitude profiles, the densities in these three panels are presented with a reversed y-axis with the largest densities at the bottom. The $T_e$ spike is not located at any specific $N_e$ as shown by Figure 2d. With increasing SZA the $T_e$ spike moves to lower altitudes and higher densities. This might partly be the reason that the $T_e$ spike is not observed at high SZA.

Based on the different ion densities and ion density ratios the most consistent relationship is between $T_e$ and $O_2^+$ density as presented in Figure 2e. The minor ion $CO_2^+$ peaks in density approximately where the $O_2^+$ density equals ~5 $10^4$ $cm^{-3}$ which is the density where the data from $T_e$ spike is located in Figure 2e. Therefore, even though $T_e$ is very well organized by the density of $O_2^+$, it is believed that this is only an indication of the location of the peak in $CO_2^+$ density. Since the maximum density of the $CO_2^+$ peaks changes with EUV intensity, the correlation between $CO_2^+$ and $T_e$ is not as clear as $O_2^+$ and $T_e$ as shown in Figure 2e. This could be indicative of the $T_e$ spike being associated with reaction rates and collision cross section of $CO_2$. Low temperature

(<400 K) cross section experiments are difficult to perform and therefore are a source of uncertainty.

The atmospheric pressure, represented by the $CO_2$ density in Figure 2f, organizes the $T_e$ spike well; the altitude variability between orbit to orbit due to atmospheric expansion and contraction is removed creating a more well-defined $T_e$ spike. This can be seen when comparing Figure 2f to Figure 2b. Starting at high pressure (low altitudes) the $T_e$ slowly increases with decreasing $N_n$ in Figure 2f. Above the $T_e$ peak, the temperature decreases much faster than seen below the peak, especially for the DD8 (green dots). This might be an artifact of the logarithmic scale or it may be associated with an atmospheric process that has a sharp change on the upper side of the $T_e$ spike. Nevertheless, the $T_e$ spike becomes 'focused' at a fixed pressure, suggesting that it is associated with plasma-neutral interactions, and the location of the $T_e$ spike is associated with a pressure balance for a particular EUV intensity.

$T_e$ is affected by heat flux and when the plasma is magnetized the main heat flux is along the magnetic field. An investigation of the $T_e$ spike has been carried out with respect to magnetic field strength and magnetic field tilt angle, but no correlation with the $T_e$ spike was found. For the data presented in Figure 2, the ions are demagnetized for almost the full altitude range. When comparing the electron collision frequency to the gyro frequency the $T_e$ spike is approximately located where such ratio is equal to one. That is, the $T_e$ spike is at the lower edge of the dynamo region but there is no clear correlation between the $T_e$ spike and electron demagnetizing altitude. The $T_e$ spike is located in the region where electrons start to be magnetized, allowing joule heating effects to provide energy to the system. At this time, the neutral wind and ion motion observations have not yet been analyzed, preventing us from evaluating if there are any altitude changes in the winds below, at, and above the location of the $T_e$ spike.

The electrons are cooled by interactions with ions and neutrals, of which the $CO_2$ vibrational excitation is the most efficient. The electron cooling rate is derived and presented in Figure2g by the thick lines. The cross section depends on the $T_e$ [Campbell, 2008] and, for each altitude profile the cooling rate using a fixed lower $T_e$ and a cooling rate for a 300 K population are presented as the thin lines in the same panel. Looking at DD2 and DD8 there is an enhanced cooling rate due to the temperature at the altitude between the horizontal dotted lines (the upper and lower boundary of the $T_e$ spike). Therefore, variations in the cross section alone cannot explain the $T_e$ spike; the enhanced temperature actually would lead to a cooler $T_e$. However, the result suggests that the accuracy of the $CO_2$ vibration cross sections may not be good enough for the temperatures and densities of interest here.

The location where there is an excess of energy to heat the electrons and where the energy is dominantly drained from the electrons by collisions is indicated in Figure 2h. In other words, the ratio between the available energy deposition (presented in Figure 2c) to the energy cooling (presented in Figure 2g) is presented in Figure 2h. This indicates that the $T_e$ spike is located where energy deposited by EUV and electron cooling due to $CO_2$ vibration is approximately equal. For DD2, this ratio is equal to one just at the upper edge of the $T_e$ spike, at lower altitudes this ratio is above the $T_e$ spike for DD8 and DD9. As discussed for DD7, which has the largest SZA, the energy deposition depends on the assumption of optical thickness. We use a higher density which the solar EUV needs to pass through when deriving energy deposition for DD7 and the result is presented

by the thin pink line in Figure 2h. As can be seen, the location where the ratio is equal to one moves to a much higher altitude, due to the uncertainty associated with large SZA during DD7.

Deriving the neutral temperature ($T_n$) is hard and often requires that the observations are made at different pressure levels (i.e. altitudes). With an elliptical orbit the descending and ascending parts of the periapsis provide enough of vertical motion to derive the $T_n$, but at periapsis, the spacecraft moves mainly horizontally resulting in higher uncertainties. High-resolution $T_n$ derived from $CO_2$, $N_2$, and $Ar$ density profiles are presented in Panel 2i by the dashed, dash-dotted, and solid lines respectively [Stone et al., 2018]. Since the altitude for the $T_e$ spike for DD2 is well away from the periapsis the $T_n$ is derived at a location where the spacecraft has a significant vertical speed. In contrast, for DD8 and DD9 the spacecraft mainly moved horizontally at this location resulting in a greater uncertainty in $T_n$. Therefore, only DD8 is included in Figure 2i.

The $T_n$ is changing significantly at the altitude of the $T_e$ spike as can be seen in Figure 2i. Below the $T_e$ spike, $CO_2$, $N_2$, and $Ar$ profiles result in similar $T_n$ but above the three temperature estimates start to deviate from eachother. The differences between the temperatures derived from the three species appear to be entirely instrumental in origin. The $Ar$ temperatures most accurately represent the temperature of the neutral atmosphere. Stone et al. [2018] discuss this behavior in more detail and therefore it is not discussed further here. Similar behavior indicating consistent $T_n$ among the various species at low altitudes but diverging $T_n$ higher up was also observed by Bougher et al. [2015] who used a different method to derive $T_n$. The fact that the $T_e$ spike is located where the different $T_n$ diverge is of interest but we will defer an explanation of this to future studies. Secondly, for DD2, there is a dip in the $T_n$ where the $T_e$ spike is located. Data from Bougher et al. [2015] indicate that $T_n$ profiles have different slopes above and below the $T_e$ spike while the $T_n$ in their model showed a smooth temperature throughout this region. Using Figure 2 and assuming the neutral dip is $\Delta T_n$ ~15 K for DD2 and $\Delta T_n$ ~5 K for DD8 the available energy fraction can be estimated through deriving $(N_n * \Delta T_n)/(N_e * \Delta T_e)$. For both deep dips in Figure 2i the ratio is ~3500, which might indicate that a small part of the decrease in available energy for the neutrals is the source for the enhanced energy in the plasma. Note that for heat convection the flow direction is opposite for neutrals (into the temperature dip) and electrons (out of the temperature peak). Since most of the energy is in the neutrals and the plasma is more or less demagnetized at this altitude, Figure 2i suggest that the source of the $T_e$ spike is associated with the neutrals.

## 3 Discussion and Conclusion

Using data from the four different DD campaigns (2, 7, 8, 9) the source of the observed $T_e$ spikes has yet to be conclusively determined. Therefore, we discuss here potential causes of these spikes and evaluate their likelihood.

The fact that the $T_e$ spikes were observed on three separate week-long DD campaigns under different plasma conditions suggests that these observations are not instrumental in origin. Ionization of the neutral flow upon the spacecraft at high speeds can result in an enhanced current observed by the LPW instrument, though such an effect should not be associated with a narrow altitude range such as observed in DD2, but instead for the full periapsis. As shown in Figure 1, detailed analysis of LPW IV-curves supports the conclusion that the $T_e$ spikes are real and well above the lower temperature resolution threshold of the instrument.

Enhanced electron heating sources can increase the $T_e$. The main energy source for thermal electrons is through collisions with photoelectrons and the suprathermal tail of the electron distribution. As Figure 2a and 2c indicate, this source is changing in the region where the $T_e$ spike is observed, but over a much larger altitude region. To explain a 300 K increase, the photoelectron energy needs to have increased by 20% in a narrow altitude region. Such an increase in the photoelectrons should be measurable by the SWEA instrument and Figure 2 does not feature such an enhancement ruling out this source for the $T_e$ spike. Furthermore, the energy deposition from EUV is smoothly changing with altitude and does not show a localized excess of energy needed to explain the $T_e$ spike.

If the electron cooling rate decreased over a narrow altitude range then this could result in enhanced $T_e$. Such changes in the electron cooling rate would be driven by changes in the neutral density or electron-$CO_2$ collision cross-section. Figure 2f demonstrates that the neutral density is lower above and higher below the $T_e$ spike, which indicates that the $N_n$ alone is not the cause of decreased cooling. There is no indication of lower neutral densities coincident with the observed $T_e$ spikes. On the contrary, the increased $T_e$ results in an enhanced cooling rate that would prevent the creation of the $T_e$ spike. Variations in electron-$CO_2$ vibrational cross sections would need to significantly deviate from the published values [Campbell et al., 2008] to decrease the cooling at the $T_e$ spike altitude. We deem it unlikely that this is the case based on our present understanding. All other sources of collisional cooling are much less effective and therefore are not viable alternatives.

For some of the DDs, precipitating protons from the solar wind as a result of multiple charge exchanges have been observed [Halekas et al., 2015]. Since not all the DDs had charge exchange protons and the amount of energy associated with them is low, they cannot be the missing source of energy either. However, the charge exchange protons start to be absorbed by the atmosphere at the same altitude of the $T_e$ spikes and their presence can therefore alter the chemistry.

Electron transport is also important for determining $T_e$ and, for charged particles, the local magnetic field can be important as well. For the altitude of interest, the ions are demagnetized and the electrons start to be demagnetized. Therefore, the analysis indicates that changes in heat flow due to magnetic field strength/direction are not important. The $T_e$ spikes are located at altitudes where the electrons become demagnetized, which corresponds to the lower dynamo region. At the time of writing, there is no indication of changes in the winds as function of altitude across the $T_e$ spike.

Neutral winds cannot directly increase the $T_e$, however heat convection is driven by temperature gradients. Since $T_n$ decreases while the $T_e$ is enhanced in the spikes, the heat convection associated with $T_n$ and $T_e$ will be in the opposite direction. If the $T_n$ convection is larger than the $T_e$ convection there might be excess energy available for $T_e$. Comparing the energy in the neutrals and plasma as described above, the ratio of energies is approximately ~3500 for both DD2 and DD8. It is interesting that, with almost 10 times difference in $N_n$, the energy fraction above is similar. This suggests that $T_n$ might be the source of the $T_e$ spike. Understanding the $T_n$ dip is outside the scope of this letter and deferred for dedicated modeling studies.

The number of in-situ $T_e$ observations at Earth in the region of interest discussed here is limited. Incoherent radars have the potential to see a $T_e$ spike in Earth's ionosphere but none were found in the literature. Early result from the AE-C mission at Earth reaching down to ~150 km needed to improve the oxygen fine structure excitation cross section to get better correlation between the heating and cooling rate [Brace et al., 1976]. However, they did not have high altitude resolution data, nor could they completely distinguish the difference between cooling and heating with the data available. Earlier, Walker [1968] demonstrated that the nitrogen vibration cross-section was critical for understanding the $T_e$ at Earth which could be indicative that we need to better understand the vibration cross sections of $CO_2$ for Mars. Omitting sounding rockets, in-situ observations by satellites (which per Kepler's laws are made at much higher speed than MAVEN) have generated plasma clouds around the satellites at corresponding altitudes so no meaningful meaurements were possible. Therefore, it is unclear if a $T_e$ spike also exists at Earth.

If the $T_e$ spike and the observed $T_n$ dip observed in DD2 are the result of atmospheric transport, this would have implications for the convection pattern and the circulation of the upper atmosphere. The observed $T_e$ spike therefore could have a significant impact on the small planet's atmosphere. Since this type of $T_e$ spike is not observed at Earth to our knowledge, the observed effect on Mars might be either common for thin atmospheres where temperature gradients are large (i.e. small scale heights) and/or for atmospheres dominated by $CO_2$ where the observation might indicate that the knowledge of the vibration cross sections is not known well enough. This letter demonstrates that further analysis of the atmosphere of Mars is needed and that such work has potential to be important to other celestial objects.

**Acknowledgments, Samples, and Data**

Work was supported by NASA funding for the MAVEN project through the Mars Exploration Program. Data used in this study are available on the NASA Planetary Data System, via https://pds.nasa.gov/.

**References**

Andersson L., R. E. Ergun, G. T. Delory, A. Eriksson, J. Westfall, H. Reed, J. McCauly, D. Summers, D. Meyers (2015), The Langmuir Probe and Waves (LPW) instrument for MAVEN, Space Science Reviews, December 2015, Volume 195, Issue 1, pp 173-198.

Andersson, L. & Ergun, R. E. (2012) Neutral wind effects on ion outflow at Mars, Earth Planet Sp, 64: 6. https://doi.org/10.5047/eps.2011.06.047

Andersson L., R. E. Ergun, and I. Stewart, (2010) The Combined Atmospheric Photochemical and Ion Tracing Code: Reproducing the Viking Landers Result and Initial Outflow Results, Volume 206, Issue 1, p. 120-129., doi: 10.1016/j.icarus.2009.07.009

Bougher et al., (2015), Early MAVEN Deep Dip campaign reveals thermosphere and ionosphere variability, Science, 06 Nov. Vol. 350, Issue 6261, aad0459, DOI: 10.1126/science.aad0459

Brace, L. H., W. R. Hoegy, H. G. Mayr, G. A. Victor, W. B. Hanson, C. A. Reber, and H. E. Hinteregger (1976), Discrepancy between electron heating and cooling rates derived from atmosphere Explorer-C measurements, *J. Geophys. Res.*, 81(31), 5421–5429, doi: 10.1029/JA081i031p05421.

Campbell, L., M. J. Brunger, and T. N. Rescigno (2008), Carbon dioxide electron cooling rates in the atmospheres of Mars and Venus, J. Geophys. Res., 113, E08008, doi: 10.1029/2008JE003099.

Chen, R.H., Cravens, T.E., Nagy, A.F., 1978. The martian ionosphere in light of the Viking observations. J. Geophys. Res. 83, 3871–3876.

Connerney, J. E. P., J. Espley, P. Lawton, S. Murphy, J. Odom, R. Oliversen, and D. Sheppard (2015), The MAVEN magnetic field investigation, Space Sci. Rev., doi:10.1007/s11214-015-0169-4.

Eparvier, F.G., Chamberlin, P.C., Woods, T.N. et al. (2015), The Solar Extreme Ultraviolet Monitor for MAVEN, Space Sci Rev, 195: 293. https://doi.org/10.1007/s11214-015-0195-2

Ergun, R. E., M. W. Morooka, L. A. Andersson, C. M. Fowler, G. T. Delory, D. J. Andrews, A. I. Eriksson, T. McEnulty, and B. M. Jakosky (2015), Dayside electron temperature and density

profiles at Mars: First results from the MAVEN Langmuir probe and waves instrument, Geophys. Res. Lett., 42, 8846–8853, doi: 10.1002/2015GL065280.

Ergun, R. E., et al. (2016), Enhanced O2+ loss at Mars due to an ambipolar electric field from electron heating, J. Geophys. Res. Space Physics, 121, 4668–4678, doi: 10.1002/2016JA022349.

Frahm, R.A. et al., (2006) Carbon dioxide photoelectron energy peaks at Mars. Icarus 182, 371 - 382.

Halekas, J. S., et al. (2015), MAVEN observations of solar wind hydrogen deposition in the atmosphere of Mars, *Geophys. Res. Lett.*, 42, 8901–8909, doi: 10.1002/2015GL064693.

Hanson, W. B., and G. P. Mantas (1988), Viking electron temperature measurements: Evidence for a magnetic field in the Martian ionosphere, J. Geophys. Res., 93(A7), 7538–7544, doi: 10.1029/JA093iA07p07538.

Jakosky, B. M., et al. (2015), The Mars Atmosphere and Volatile Evolution (MAVEN) mission, Space Sci. Rev., doi:10.1007/s11214-015-0139-x.

Ma, Y. J., et al. (2017), Variations of the Martian plasma environment during the ICME passage on 8 March 2015: A time-dependent MHD study, J. Geophys. Res. Space Physics, 122, 1714–1730, doi: 10.1002/2016JA023402.

Mahaffy, P. R., et al. (2014), The neutral gas and ion mass spectrometer on the Mars Atmosphere and Volatile Evolution Mission, Space Sci. Rev.,185, doi:10.1007/s11214-11014-10091-11211.

Mitchell, D. L., et al. (2016), The MAVEN Solar Wind Electron Analyzer, Space Sci. Rev., 200(1–4), 495–528.

Peterson, W. K., et al. (2016), Photoelectrons and solar ionizing radiation at Mars: Predictions versus MAVEN observations, J. Geophys. Res. Space Physics, 121, 8859–8870, doi:10.1002/2016JA022677.

Rohrbaugh, R.P., Nisbet, J.S., Bleuler, E., Herman, J.R., (1979). The effect of energetically produced O2+ on the ion temperatures of the martian thermosphere. J. Geophys. Res. 84, 3327–3338.

Sakai, S., et al. (2016), Electron energetics in the Martian dayside ionosphere: Model comparisons with MAVEN data, J. Geophys. Res. Space Physics, 121, 7049–7066, doi: 10.1002/2016JA022782.

Schunk, R. W., and A. F. Nagy (1980), Ionospheres of the terrestrial planets, Rev. Geophys., 18(4), 813–852, doi: 10.1029/RG018i004p00813.

Strangeway, R. J. (1996), Collisional Joule dissipation in the ionosphere of Venus: The importance of electron heat conduction, J. Geophys. Res., 101(A2), 2279–2295, doi: 10.1029/95JA02587.

Stone, S. W., Yelle, R. V., Benna, M., Elrod, M. K., & Mahaffy, P. R. (2018). Thermal structure of the Martian upper atmosphere from MAVEN NGIMS. Journal of Geophysical Research: Planets, 123, 2842–2867. https://doi.org/10.1029/2018JE005559.

Walker J. C. G. (1968), Electron and nitrogen vibrational temperature in the E-region of the ionosphere, Planetary and Space Science, Volume 16, Issue 3, p. 321-327, doi:10.1016/0032-0633(68)90006-8.

**Table** 1: The characteristics of the four Deep Dip events

| <160 km | YY-MM of DD | SZA [$^o$] | LT [hour] | Lat [$^o$] | Periapsis [km] | $T_e$ peak | Magnitude $dT_e$ [K] | Width [km] |
|---|---|---|---|---|---|---|---|---|
| DD2 | 2015-04 | 1 - 23 | 11 - 13 | -17 - 10 | ~133 | Yes | 300 | 10 |
| DD8 | 2017-10 | 21 - 33 | 13 - 14 | 2 - 34 | ~127 | Yes | 300 | 6 |
| DD9 | 2018-04 | 42 - 70 | 13 - 16 | -63 - -36 | ~127 | Yes | 300 | ~6 |
| DD7 | 2017-08 | 85 - 90 | 17 - 18 | 49 - 74 | ~128 | No | Nan | Nan |

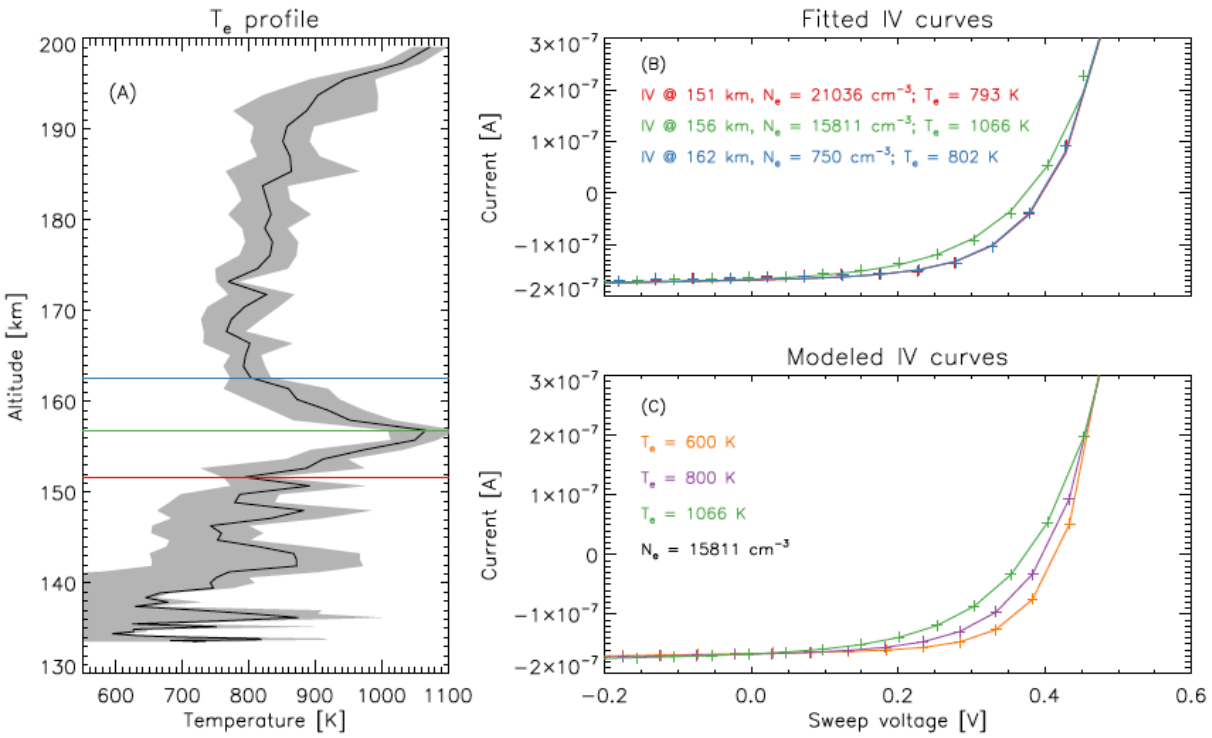


**Figure 1**: Electron IV-sweep demonstrating that the $T_e$ spike is unlikely to be an instrument effect. The derived $T_e$ from one inbound periapsis segment from DD2 is presented in panel a. The region of the IV-sweep where temperature is extracted is presented in panel b. The altitude of the sweep is color coded and shown in panel a based on the horizontal lines. Panel c replots the $T_e$ peak IV-sweep (green line) and then two IV-sweeps representing the same density but different temperatures highlighting that $T_e$ is sufficiently resolved.

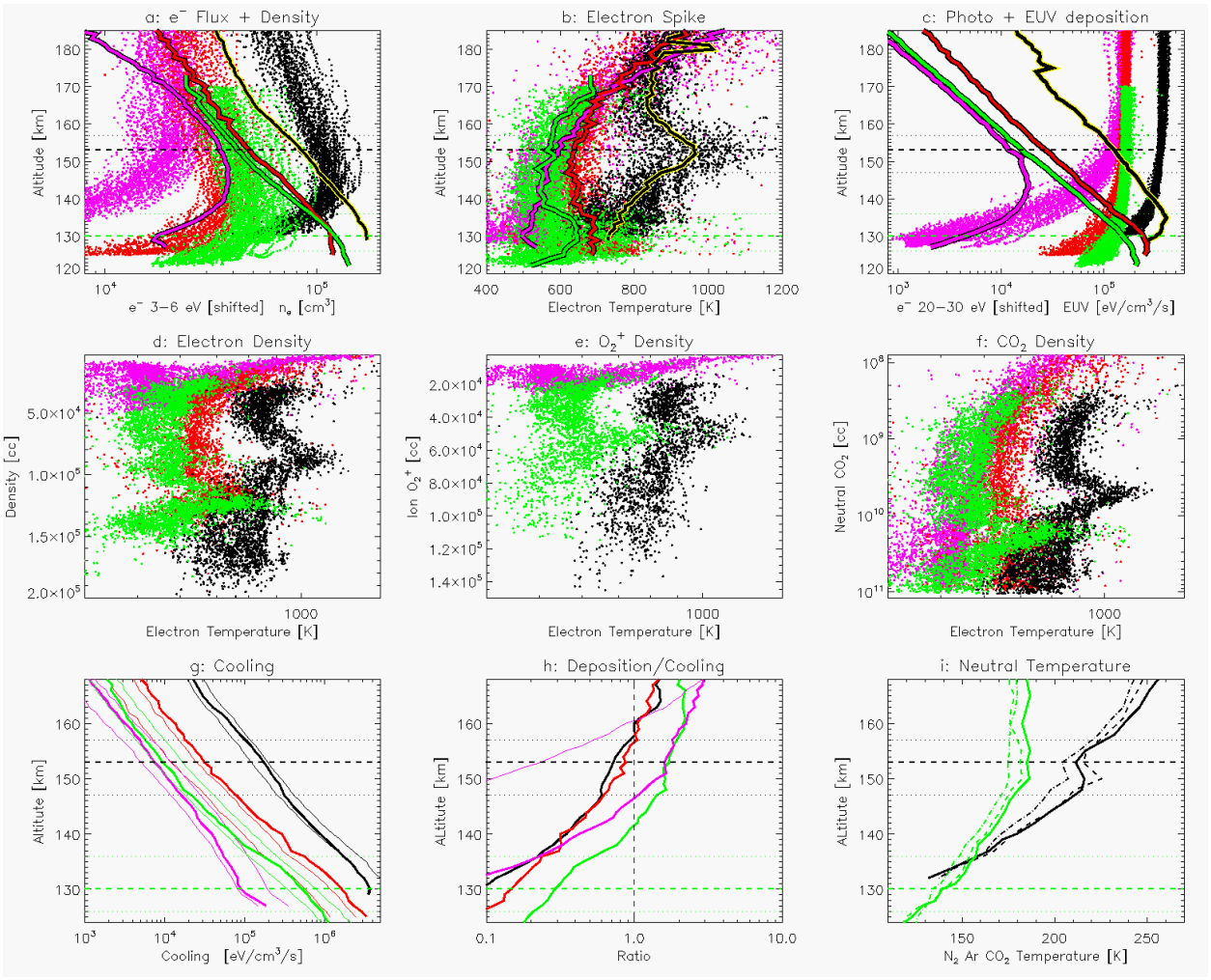


**Figure 2**: The electron $T_e$ spike for DD2, DD8, DD9, and DD7 compared with different plasma and neutral parameters with black, green, red, and pink colors, respectively. Each panel axis is labeled and the details of the Figure are explained in the body of the text. The altitude envelope of the $T_e$ spike for DD2 and DD8 is marked by the horizontal dotted lines for the panels which have altitude on the y-axis for ease of comparison between the panels.